


Lattice Vibrations and Molecular Conformations in a Plastic Crystal: A Path to Solid-State Cooling Materials

Ares Sanuy^{1,2}, Carlos Escorihuela-Sayalero^{1,2}, Pol Lloveras^{1,2}, Josep-Lluís Tamarit^{1,2},
Luis Carlos Pardo^{1,2,*} and Claudio Cazorla^{1,2,†}

¹Group of Characterization of Materials, Departament de Física, *Universitat Politècnica de Catalunya, Campus Diagonal-Besòs, Av. Eduard Maristany 10–14, 08019 Barcelona, Spain*

²Barcelona Research Center in Multiscale Science and Engineering, *Universitat Politècnica de Catalunya, Campus Diagonal-Besòs, Av. Eduard Maristany 10–14, 08019 Barcelona, Spain*

 (Received 22 March 2025; revised 18 July 2025; accepted 29 August 2025; published 23 September 2025)

In recent years, orientationally disordered crystals, or plastic crystals, have transformed the field of solid-state cooling due to the significant latent heat and entropy changes associated with their temperature-induced molecular order-disorder phase transition, which can produce colossal caloric effects under external field stimuli. However, the molecular mechanisms underlying these huge caloric effects remain inadequately understood and general principles for enhancing the performance of caloric plastic crystals are lacking. Previous studies have predominantly focused on molecular rotations, overlooking other potentially critical factors, such as lattice vibrations and molecular conformations. In this study, we employ classical molecular dynamics (MD) simulations to both replicate and elucidate the microscopic origins of the experimentally observed colossal barocaloric (BC) effects—those driven by hydrostatic pressure—in the archetypal plastic crystal neopentyl glycol (NPG). Our MD simulations demonstrate that in NPG, the combined BC response and phase-transition entropy changes arising from lattice vibrations and molecular conformations are nearly equal to those from molecular reorientations. These findings suggest that alongside hydrogen bonding—which directly impacts molecular rotational dynamics—lattice vibrational and molecular structural features, often overlooked, must be integrated into the rational design and modeling of advanced caloric plastic crystals. These insights are not only of significant fundamental interest but also essential for driving the development of next-generation solid-state refrigeration technologies.

DOI: [10.1103/bknr-9rmn](https://doi.org/10.1103/bknr-9rmn)

I. INTRODUCTION

Solid-state cooling methods offer energy-efficient and environmentally friendly alternatives to conventional refrigeration technologies, which rely on compression cycles of greenhouse gases [1–7]. Caloric materials, when subjected to moderate external field variations (e.g., magnetic, electric, mechanical, or light irradiation), exhibit significant adiabatic temperature changes ($|\Delta T| \sim 1 - 10$ K) due to phase transformations that involve substantial isothermal entropy changes ($|\Delta S| \sim 10 - 100 \text{ J K}^{-1} \text{ kg}^{-1}$). Solid-state cooling leverages these caloric effects to design efficient refrigeration cycles.

From a practical standpoint, achieving responsive and efficient thermal devices under repeated application and removal of driving fields requires both large and reversible $|\Delta T|$ and $|\Delta S|$. Among the various caloric effects, mechanocaloric responses induced by uniaxial stress (elastocaloric) and hydrostatic pressure (barocaloric, BC) are particularly promising due to their substantial figures of merit [8–13].

Recently, colossal and reversible BC effects ($|\Delta S| \geq 100 \text{ J K}^{-1} \text{ kg}^{-1}$) have been observed in several families of plastic crystals undergoing molecular order-disorder (OD) phase transitions under pressure changes of the order of 0.1 GPa [14–18]. Prominent examples include neopentane derivatives [19–22], adamantane-based compounds [23,24], carboranes [25], and closo-borate crystals [26,27]. These materials constitute a pivotal class of disordered systems driving leading-edge advancements in barocaloric refrigeration technology [13,28]. However, a complete and fundamental understanding of the physical mechanisms behind the colossal BC effects observed in plastic crystals remains elusive.

*Contact author: luis.carlos.pardo@upc.edu

†Contact author: claudio.cazorla@upc.edu

Published by the American Physical Society under the terms of the [Creative Commons Attribution 4.0 International](https://creativecommons.org/licenses/by/4.0/) license. Further distribution of this work must maintain attribution to the author(s) and the published article's title, journal citation, and DOI.

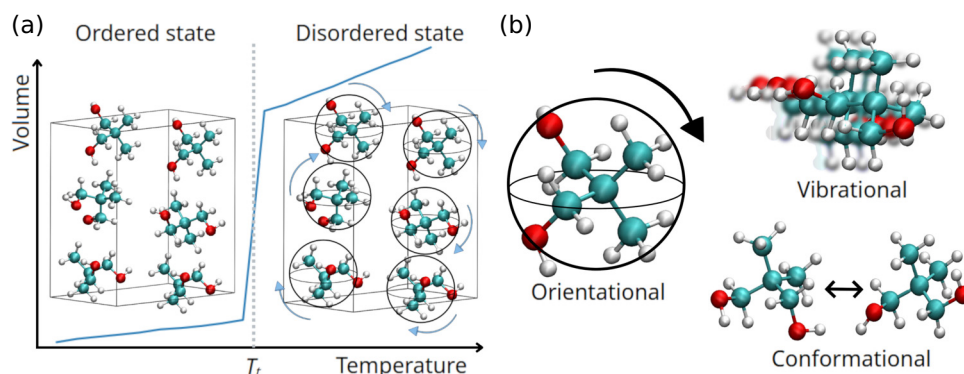


FIG. 1. A sketch of the T -induced order-disorder (OD) phase transition in neopentyl glycol (NPG) and different sources of entropy in the high- T disordered state. (a) Below the transition temperature, T_t , NPG presents an ordered phase in which only molecular vibrations and lattice phonons contribute to its entropy. Above T_t , NPG becomes orientationally disordered and, besides molecular vibrations and lattice phonons, the angular degrees of freedom, including possible molecular orientations and conformations, also contribute to the system entropy. The OD phase transition is accompanied by a large change in volume and entropy. (b) A representation of the three possible sources of entropy in the high- T disordered phase of NPG.

To date, the large $|\Delta T|$ and $|\Delta S|$ measured in plastic crystals have been primarily attributed to substantial entropy changes arising from molecular orientational disorder [29–32]. This molecular disorder emerges at high temperatures and is typically accompanied by an enormous volume increase of the order of 10% [19–22] [Fig. 1(a)]. Notably, hydrogen-bond interactions between molecules have been found to play a crucial role in the orientational dynamics, hindering or facilitating the molecular reorientations depending on whether these interactions are reinforced or weakened [29,30,33]. As a result, the origin of colossal BC effects has been predominantly linked to orientational dynamics and hydrogen bonding, often overlooking other potential sources of entropy such as lattice vibrations and molecular conformations [Fig. 1(b)].

Interestingly, recent experimental and theoretical studies have highlighted the significant contributions of vibrational and molecular conformational degrees of freedom to the phase-transition entropy change in plastic crystals and related orientationally disordered materials, such as hybrid organic-inorganic perovskites [27,34–38]. For instance, approximately 60% of the reversible $|\Delta S|$ measured in adamantane has been attributed solely to vibrational effects [36]. Similarly, in the case of the monocarba-closo-dodecaborate $\text{LiCB}_{11}\text{H}_{12}$, only about 30% of the phase-transition entropy change is associated with molecular reorientations [27]. Moreover, the conformational flexibility and soft nature of hydrocarbon chains, which enable numerous degenerate molecular configurations in the high- T disordered phase, have been identified as the primary mechanisms driving substantial BC effects in two-dimensional metal-halide perovskites [39,40] and hybrid organic-inorganic halide salts [41].

These findings suggest that molecular reorientations alone might not fully account for the colossal BC effects

measured in plastic crystals. This possibility underscores the urgent need to rigorously identify and quantify all potential sources of entropy change in such materials. Addressing this challenge is crucial for two primary reasons: first, to validate and potentially improve the phenomenological free-energy models currently used to describe OD phase transitions in molecular crystals [31, 32]; and, second, to accelerate the rational design and development of new energy-efficient solid-state cooling materials, thus paving the way for their broader technological adoption.

In this study, we have employed classical molecular dynamics (MD) simulations to uncover the microscopic origins of the experimentally observed colossal BC effects in the archetypal plastic crystal neopentyl glycol $(\text{CH}_3)_2\text{C}(\text{CH}_2\text{OH})_2$ (NPG). Our simulations reveal that the combined contributions of lattice vibrations and molecular conformations to the phase-transition entropy change and BC descriptor ΔS are comparable in magnitude to those from molecular reorientations. These findings underscore the importance of incorporating not only molecular rotational dynamics but also structural features and lattice phonons into the microscopic understanding and smart engineering of caloric plastic crystals.

The structure of this paper is as follows. First, we provide an overview of the employed simulation and entropy-evaluation methods, which have recently been introduced in the literature [27,34,35]. Next, we present our results for the OD phase transition and BC effects in NPG, discussing their alignment with the reported experimental data. This is followed by a detailed analysis of the different contributions to the calculated entropy change and BC performance. Finally, we summarize our main findings in Sec. V.

II. COMPUTATIONAL APPROACH

A. Simulations overview and general definitions

We have conducted comprehensive classical MD simulations in the NPT ensemble (i.e., fixed number of particles N , pressure P , and temperature T) for NPG across a wide thermodynamic range. Our NPT -MD simulations have employed a CHARMM-type force field comprising bonded (e.g., angle bending, bond stretching, and dihedral torsion) and nonbonded (i.e., van der Waals and electrostatic) interactions [42–44] (see the Supplemental Material [45]). This classical interatomic potential accurately captures the physical behavior of NPG at low and high temperatures (see Sec. III). Further details of our NPT -MD simulations can be found in Sec. VI.

The total entropy of the low- T ordered and high- T disordered phases of NPG, S , were determined as a function of pressure and temperature using the relation

$$S(P, T) = S_{\text{vib}}(P, T) + S_{\text{ang}}(P, T), \quad (1)$$

where S_{vib} is the entropy contribution from the lattice vibrations and S_{ang} is the contribution from the molecular angular degrees of freedom.

Likewise, the molecular angular entropy has been evaluated using the expression

$$S_{\text{ang}}(P, T) = S_{\text{ori}}(P, T) + S_{\text{conf}}(P, T), \quad (2)$$

where S_{ori} is the entropy contribution from the orientational degrees of freedom and S_{conf} is the contribution from the molecular conformational degrees of freedom. This decomposition of S_{ang} allows us to avoid constructing a high-dimensional joint angular probability distribution, which would be prohibitively sparse and therefore unsuitable for robust estimation of the angular entropy [46,47]. In Sec. IV, we quantitatively discuss the impact of this approximation, namely, decoupling of the orientational and conformational molecular degrees of freedom, on the calculation of S_{ang} . Similarly, molecule-molecule orientational correlations have been neglected in the computation of the angular entropy, even though such correlations may indeed be present in the system, particularly across the phase transition. This choice is justified by their expected minor contribution, which is on the order of $10 \text{ J K}^{-1} \text{ kg}^{-1}$ [34,48] (i.e., approximately one order of magnitude smaller than S_{ori} ; see Sec. IV).

In this study, we have primarily focused on reproducing and understanding, at the molecular level, the origins of the experimental colossal BC effects measured in NPG. In this context, a physical quantity of interest is the OD phase-transition entropy change, defined as

$$\Delta S_t = \Delta S_t^{\text{vib}} + \Delta S_t^{\text{ori}} + \Delta S_t^{\text{conf}}, \quad (3)$$

where $\Delta S_t^x \equiv S_x(\text{disordered}) - S_x(\text{ordered})$ and all the entropy terms are evaluated at the phase-transition temperature, T_t , corresponding to a fixed pressure. The main improvement of this ΔS_t definition, compared to those in previous works [27,35], is the inclusion of molecular conformational changes (ΔS_t^{conf}).

B. Vibrational entropy

The vibrational density of states (VDOS) $\rho(\omega)$, where ω represents the lattice vibration frequency, provides information on the phonon spectrum of a crystal and allows us to estimate key thermodynamic quantities such as the vibrational free energy, F_{vib} and the vibrational entropy, $S_{\text{vib}} = -\partial F_{\text{vib}}/\partial T$. A possible manner of calculating $\rho(\omega)$ from the outputs of NPT -MD simulations consists in estimating the Fourier transform of the velocity autocorrelation function (VACF) [35,49,50], defined as

$$\text{VACF}(t) = \langle \mathbf{v}(0) \cdot \mathbf{v}(t) \rangle = \frac{1}{N} \sum_i^N \mathbf{v}_i(0) \cdot \mathbf{v}_i(t), \quad (4)$$

where $\mathbf{v}_i(t)$ represents the velocity of the i th particle and $\langle \dots \rangle$ is the statistical average performed in the NPT ensemble. Subsequently, the VDOS can be estimated as

$$\rho(\omega) = \int_0^\infty \text{VACF}(t) e^{i\omega t} dt, \quad (5)$$

which fulfills the normalization condition:

$$\int_0^\infty \rho(\omega) d\omega = 3N, \quad (6)$$

where $3N$ is the number of real and positively defined phonon-frequency branches of the crystal.

Upon determination of ρ , the vibrational free energy can be straightforwardly estimated as a function of pressure and temperature using the formula [51]

$$F_{\text{vib}}(P, T) = k_B T \times \int_0^\infty \ln \left[2 \sinh \left(\frac{\hbar\omega}{2k_B T} \right) \right] \rho(\omega) d\omega, \quad (7)$$

where k_B is Boltzmann's constant and $\rho(\omega)$ depends both on P and T . Consistently, the vibrational entropy adopts the expression

$$S_{\text{vib}}(P, T) = - \int_0^\infty k_B \ln \left[2 \sinh \left(\frac{\hbar\omega}{2k_B T} \right) \right] \rho(\omega) d\omega + \int_0^\infty \frac{\hbar\omega}{2T} \tanh^{-1} \left(\frac{\hbar\omega}{2k_B T} \right) \rho(\omega) d\omega. \quad (8)$$

C. Molecular orientational entropy

For a continuous random variable x with probability density $f(x)$, its entropy is defined as [52]:

$$S = - \int_X f(x) \log f(x) dx, \quad (9)$$

where the integral runs over all possible values of x . If x represents a microstate characterizing a particular thermodynamic macrostate, then the following Gibbs entropy can be defined for the system of interest [53]:

$$S_G = -k_B \int_X f(x) \log f(x) dx. \quad (10)$$

In an orientationally disordered crystal, molecules rotate in a quasirandom manner and their orientation with respect to a static reference system can be described by the three angles θ , ϕ , and ψ (see Sec. III C). By assuming the NPG molecules in the crystal to rotate independently one from the other and as rigid bodies [34], one can estimate a probability density function for their orientation, $f(\theta, \phi, \psi)$, from the atomistic trajectories generated during long *NPT*-MD simulations. In this case, the following three-dimensional molecular orientational entropy can be defined as [46,47,54,55]

$$S_{\text{ori}}(P, T) = S_{\text{ori}}^0(P, T) - k_B \int f(\theta, \phi, \psi) \log [f(\theta, \phi, \psi)] \times d \cos(\theta) d\phi d\psi, \quad (11)$$

where S_{ori}^0 is a reference orientational entropy term. (For a fluid, the value of this reference entropy term matches that of an ideal gas under the same temperature and density conditions as the system of interest [46,47,54,55]; however, for an orientationally disordered solid, this reference term is not as straightforward to define [35].)

In practice, the calculation of S_{ori} entails the construction of histograms for which the continuous polar variables are discretized, $\{\theta, \phi, \psi\} \rightarrow \{\theta_i, \phi_i, \psi_i\}$. Accordingly, one may define the bin probabilities [52]:

$$p_i(\theta_i, \phi_i, \psi_i) \approx f(\theta_i, \phi_i, \psi_i) \times \Delta \cos(\theta) \Delta \phi \Delta \psi, \quad (12)$$

where $\Delta \cos(\theta) \Delta \phi \Delta \psi$ is the volume of a histogram bin (selected to be constant in this study). Consistently, one can rewrite the molecular orientational entropy in the discretized form [27,34,35,52]

$$\Delta S_{\text{ori}}(P, T) = -k_B \sum_i p_i \log p_i + k_B \log [\Delta \cos(\theta) \Delta \phi \Delta \psi], \quad (13)$$

where the value of the reference entropy term in Eq. (11) has been offset.

D. Molecular conformational entropy

At finite temperatures, NPG molecules may undergo conformational changes that contribute to the total entropy, S_{conf} . The dihedral angles α and β (see Sec. III D) can be used to monitor such conformational molecular changes. Analogously to the case of the orientational entropy, a probability density function can be estimated for these molecular dihedral angles from the atomistic trajectories generated during long *NPT*-MD simulations, $f(\alpha, \beta)$. Therefore, a bin probability can be defined, $p_i(\alpha_i, \beta_i) \approx f(\alpha_i, \beta_i) \Delta \alpha \Delta \beta$, leading to the conformational entropy expression

$$\Delta S_{\text{conf}}(P, T) = -k_B \sum_i p_i \log p_i + k_B \log (\Delta \alpha \Delta \beta), \quad (14)$$

where $\Delta \alpha \Delta \beta$ is the fixed area of a histogram bin and the corresponding reference entropy term is offset, similar to ΔS_{ori} . Without loss of generality and consistent with the observations [56], the conformational and orientational entropies of the low-temperature ordered phase of NPG are assumed to be negligible in this study.

III. RESULTS

A. OD phase transition in NPG

In Fig. 2, we present the P - T phase diagram of NPG along with key thermodynamic properties derived from *NPT*-MD simulations. The low-temperature ordered phase exhibits monoclinic symmetry (space group $P2_1/n$) [56], while the high-temperature disordered phase adopts a cubic (face-centered) lattice, in consistent agreement with experimental observations [19,20]. The onset of molecular reorientations in the high-temperature disordered phase is marked by a significant and abrupt volume increase [Fig. 2(a)]. For instance, at zero pressure, the volume change at the phase transition corresponds to approximately 8.5% of the volume of the low-temperature ordered phase [Figs. 2(a), 2(c)]. This relative volume expansion decreases progressively under compression (e.g., $\Delta V_t/V \approx 3\%$ at $P = 0.5$ GPa).

It is found that our *NPT*-MD simulations significantly overestimate the experimental volume change observed during the OD phase transition [Fig. 2(c)]. However, when considering the numerical uncertainties associated with ΔV_t , both theory and experiments are in reasonable agreement. It is worth noting that near phase-transition points, the volume of the system fluctuates quite appreciably in our *NPT*-MD simulations, thus resulting in sizable error bars [Fig. 2(c)].

The P - T phase diagram of NPG has been estimated up to a pressure of 0.5 GPa [Fig. 2(b)]. The slope of the calculated phase boundary is positive and nearly constant within the compression range $0 \leq P \leq 0.2$ GPa, with a value of $dT_t/dP = 125 \pm 10$ K GPa⁻¹. At higher

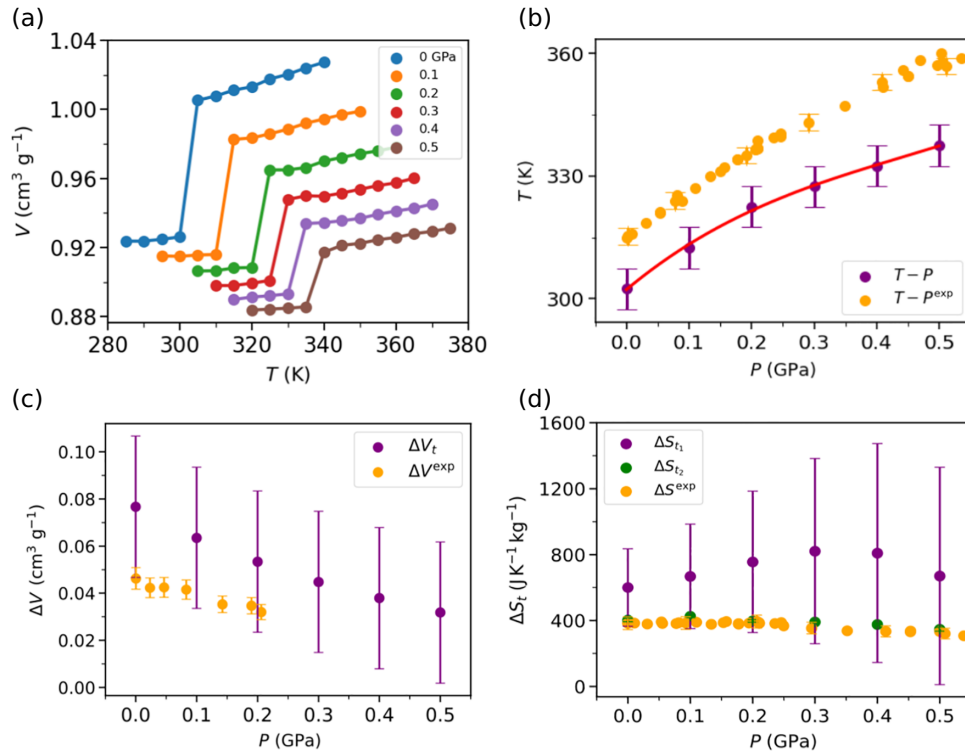


FIG. 2. The simulated OD phase transition in NPG expressed as a function of pressure and temperature. (a) The volume evolution obtained from the NPT -MD simulations. The solid lines are guides for the eye. (b) The transition temperature expressed as a function of pressure (violet dots); experimental data (orange dots) [19] are shown for comparison. The red line corresponds to a third-order polynomial fit to the simulation data of the form $T = 138.89P^3 - 184.52P^2 + 127.78P + 302.26$, where the temperature and pressure are in units of kelvin and gigapascals, respectively. (c) The transition volume change expressed as a function of pressure (violet dots); experimental data (orange dots) [19] are shown for comparison. (d) The transition entropy change expressed as a function of pressure (violet and green dots). ΔS_{t_1} and ΔS_{t_2} have been estimated indirectly using the Clausius-Clapeyron relation and directly from the NPT -MD simulations, respectively. Experimental data (orange dots) [19] are shown for comparison.

pressures ($0.3 \leq P \leq 0.5$ GPa), the induced variation of the transition temperature decreases noticeably, reaching approximately $85 \pm 10 \text{ K GPa}^{-1}$. In general, our NPT -MD simulations underestimate the experimental transition temperature (measured upon heating) by about 15–20 K [19], depending on pressure. However, at pressures below 0.2 GPa, the slope of the experimental phase boundary ($dT_t^{\text{exp}}/dP = 113 \pm 5 \text{ K GPa}^{-1}$ [19]) is in very good agreement with the value predicted by our simulations. At higher pressures, the agreement between the experimental and theoretical phase-boundary slopes diminishes, highlighting the potential limitations of the employed force field.

In Fig. 2(d), we compare the experimental and calculated transition entropy changes, ΔS_t , as a function of pressure. The first theoretical estimate, ΔS_{t_1} , has been derived using the well-known Clausius-Clapeyron equation:

$$\Delta S_{t_1} = \left(\frac{dT_t}{dP} \right)^{-1} \Delta V_t, \quad (15)$$

where ΔV_t represents the phase-transition volume change. This calculation relies on the simulation data shown in Figs. 2(a)–2(c). The second theoretical estimate, ΔS_{t_2} , has been directly obtained from the NPT -MD simulations by leveraging the Gibbs free-energy equality of the ordered and disordered phases at the phase-transition temperature. Using this approach, this quantity has been computed as $\Delta S_{t_2} = (\Delta U_t + P\Delta V_t)/T_t$, where U denotes the internal energy of the system. Meanwhile, the experimental value, ΔS_{exp} , has been determined from calorimetry measurements [19].

Several conclusions can be drawn from the ΔS_t results presented in Fig. 2(d). First, the two theoretical estimates, ΔS_{t_1} and ΔS_{t_2} , are consistent with each other within their respective numerical uncertainties. However, ΔS_{t_1} is associated with significantly larger error bars, primarily due to pronounced system volume fluctuations near the phase-transition points in the NPT -MD simulations and numerical uncertainties of the calculated phase-boundary slope. These findings highlight that entropy changes estimated via the Clausius-Clapeyron equation can be subject to sizable inaccuracies and, therefore, may not be reliable for

precise quantitative analysis. Second, the experimentally measured phase-transition entropy change shows excellent agreement with the computed ΔS_{t_2} across the entire pressure range examined. For instance, at ambient pressure, the experimental value is $383 \pm 40 \text{ J K}^{-1} \text{ kg}^{-1}$ [19], while the corresponding theoretical estimate is approximately $400 \text{ J K}^{-1} \text{ kg}^{-1}$ (see Table I). This remarkable level of agreement between experimental and theoretical values of ΔS_t , irrespective of pressure, provides strong quantitative validation for the subsequent barocaloric analysis presented in Sec. III E.

B. Vibrational changes across the OD phase transition

In Fig. 3(a), we present the vibrational density of states (VDOS) for the ordered ($T = 315 \text{ K}$) and disordered ($T = 360 \text{ K}$) phases of NPG at zero pressure, as obtained from our *NPT*-MD simulations. The VDOS displays three distinct frequency regimes: low ($0 \leq \omega \leq 20 \text{ THz}$), medium ($20 \leq \omega \leq 35 \text{ THz}$), and high ($35 \leq \omega \leq 50 \text{ THz}$). Across all frequency ranges, the VDOS peaks for the low- T ordered phase are sharper and more distinct, suggesting a lower degree of anharmonicity compared to the high- T disordered phase [57,58]. The heightened anharmonicity of the disordered phase contributes to an increased vibrational entropy (S_{vib}). In Sec. IV, we present a detailed quantitative analysis of the variation in S_{vib} associated with the OD phase transition. Here, we focus on the fundamental vibrational differences between the low- T ordered and high- T disordered phases of NPG.

Under near-ambient conditions, the low-frequency range is the most relevant for evaluating variations in S_{vib} , as inferred from Eq. (8). Specifically, we focus our analysis on the total and partial VDOS within the range $0 \leq \omega \leq 10 \text{ THz}$, which contributes most significantly to entropy changes. For completeness, however, we extend our VDOS analysis to the entire low-frequency interval, as shown in Figs. 3(b)–3(e).

In the $0 \leq \omega \leq 5 \text{ THz}$ interval, the high- T disordered phase exhibits a greater accumulation of vibrational states than the low- T ordered phase. Specifically, the VDOS surge near $\omega = 0 \text{ THz}$ is more pronounced in the disordered phase and its decline following the first local maximum is less steep [Fig. 3(b)]. Within this frequency range, the vibrational contribution from the C atoms is significantly larger than that of other atoms [Figs. 3(c)–3(e)]. However, the differences in VDOS between the ordered and disordered phases are more prominently influenced by the H and O atoms, as the C atom DOS remains largely similar for both phases.

In the $5 \leq \omega \leq 10 \text{ THz}$ interval, the VDOS of the low- T ordered phase exhibits two distinct peaks, whereas only one peak is observed for the high- T disordered phase [Fig. 3(b)]. Furthermore, the local minima in the VDOS are shallower in the disordered phase compared to the

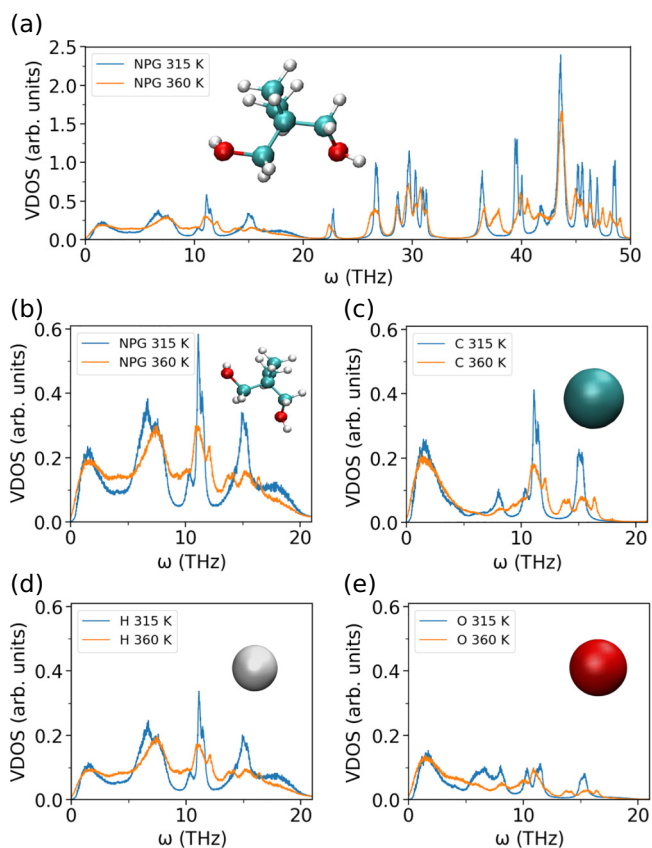


FIG. 3. The vibrational density of states (VDOS) estimated for the ordered and disordered phases of NPG. (a) The total VDOS calculated for a broad frequency range at zero pressure and temperatures above and below T_t . (b) The total VDOS calculated in the low-frequency range. (c)–(e) The partial VDOS corresponding to (c) carbon, (d) hydrogen, and (e) oxygen atoms.

ordered phase. Comparisons between the total and partial VDOS [Figs. 3(b)–3(e)] reveal that the attenuation of vibrational peaks in the disordered phase is primarily driven by contributions from the H atoms.

Finally, in the $10 \leq \omega \leq 20 \text{ THz}$ interval, the high- T disordered phase displays a greater number of VDOS peaks compared to the low- T ordered phase, although these peaks are lower in intensity. Comparisons between the total and partial VDOS [Figs. 3(b)–3(e)] indicate that the emergence of additional vibrational peaks in the disordered phase is predominantly influenced by contributions from the C and H atoms.

Notably, our zero-pressure VDOS calculations show fairly good agreement with the available experimental data. Raman spectroscopic measurements for the ordered phase of NPG at $T = 296 \text{ K}$ report six distinct peaks in the frequency range $5 \leq \omega \leq 20 \text{ THz}$, located at approximately 7, 10, 11, 12, 16, and 17 THz [59]. Similarly, our VDOS calculations at $T = 315 \text{ K}$ also reveal six peaks within the same frequency range, at approximately 7, 11, 12, 13, 15, and 18 THz [Fig. 3(b)]. These findings confirm

that our *NPT*-MD simulations provide a realistic description of the vibrational properties of NPG, at least for the low- T ordered phase, within the frequency range that is relevant to this study.

C. Orientational degrees of freedom

In plastic crystals, orientational disorder resulting from molecular rotations emerges at high temperatures and is typically accompanied by a substantial volume increase [Fig. 1(a)] [19–22]. In Sec. IV, we provide a detailed quantitative analysis of S_{ori} estimated across the OD phase transition. Here, we concentrate on the molecular orientational differences between the low- T ordered and high- T disordered phases of NPG.

To study the orientation of the NPG molecules, which in this work are assumed to rotate independently of each other and as rigid bodies [34], we define a co-mobile reference system for each molecule as follows [Fig. 4(a)]. The origin is placed at the C atom nearest to the molecular center of mass, which is exclusively bonded to other C atoms. The z axis is defined along the direction connecting this central C atom to another C atom in a hydroxyl group (denoted as the molecular polar axis). The x axis is chosen perpendicular to the plane containing the z axis and the two C atoms closer to the reference system origin. Finally, the y axis is determined as perpendicular to the x - z plane [Fig. 4(a)].

As a molecule begins to rotate, its change in orientation relative to a fixed reference system (e.g., the co-mobile reference system at the launch of the simulation) can be tracked by calculating the three angles θ , ϕ , and ψ . These

angles are illustrated in Fig. 4(a) and their definitions follow standard polar coordinates and Euler conventions [46,47]. It is important to note that the choice of the fixed reference system is arbitrary, as it does not affect the resulting angular probability distribution diagrams (except for a uniform constant shift).

In Figs. 4(b)–4(e), we present bidimensional histograms of the polar angle θ as a function of the rotational angles ϕ and ψ , which together completely define the orientation of NPG molecules. These histograms are shown for both the low- T ordered [Figs. 4(b), 4(d)] and high- T disordered [Figs. 4(c), 4(e)] phases. The averages have been computed over 1000 system configurations extracted from the *NPT*-MD simulations at 0.5 ps intervals, to minimize the correlations between the samples and improve the statistics. In the orientational maps, the red regions indicate high-probability molecular orientations, while the blue regions indicate low-probability molecular orientations.

As expected, the number of possible molecular orientations in the high- T disordered phase is greater than in the low- T ordered phase. In the ordered phase, four distinct reddish spots are observed in the ϕ - $\cos\theta$ and ψ - $\cos\theta$ histograms. These spots correspond to the specific orientations of the four molecules within the monoclinic unit cell ($Z = 4$). In contrast, the disordered phase exhibits a more complex behavior. Specifically, the molecular polar axis adopts three distinct orientations, aligning approximately with the angles $\theta = 0^\circ$, 90° , and 180° . Furthermore, the preferred molecular orientations are threefold for apical configurations ($\cos\theta = -1, 1$) and sixfold within the equatorial plane ($\cos\theta = 0$), totaling to 12. Consistently,

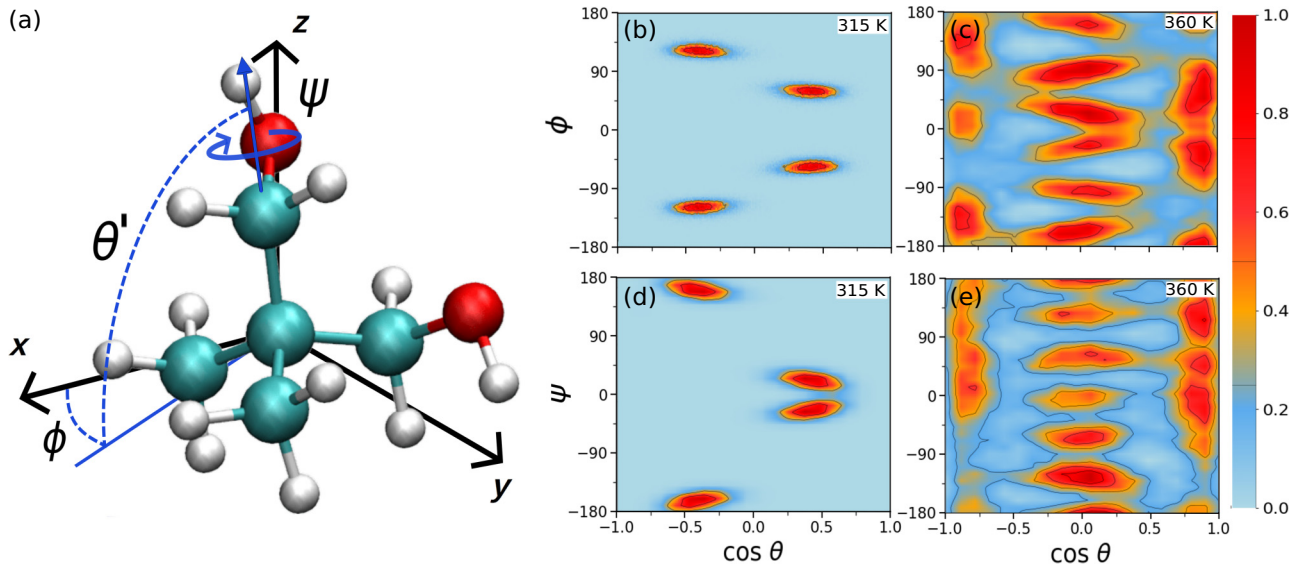


FIG. 4. The molecular orientational degrees of freedom in the ordered and disordered phases of NPG. (a) A representation of the three angles θ , ϕ , and ψ describing the orientation of NPG molecules in a fixed reference system ($\theta' \equiv \frac{\pi}{2} - \theta$). The black (blue) lines represent the fixed reference system (the co-mobile molecular polar axis and its projection on the fixed x - y plane). (b)–(e) Average orientational angle histograms obtained from *NPT*-MD simulations at temperatures (b), (d) below (315 K) and (c), (e) above (360 K) the phase-transition point at zero pressure.

this number of preferred molecular orientations is equal to the number of nearest neighbors in the face-centered-crystal arrangement of the high- T disordered phase.

An important observation is that in the low- T ordered phase, the high-probability orientation spots are isolated [Figs. 4(b), 4(d)]. The absence of orientational paths connecting these spots effectively renders the probability of a molecule adopting a different orientation from its initial one to be zero. In contrast, the high- T disordered phase displays a fundamentally different pattern. As shown in Figs. 4(c), 4(e), the preferred molecular orientations are interconnected by nonzero probability paths, indicating that molecular orientations can evolve over time via transitions along these paths. These orientational transitions are not random but, rather, well-defined, unlike in an ideal molecular rotor, where all three-dimensional orientations are equally probable and no specific preferred orientations or transition paths exist [35].

D. Conformational degrees of freedom

Molecules in plastic crystals exhibit a degree of flexibility, allowing them to undergo conformational changes driven by thermal excitations and intermolecular interactions, both in the low- T ordered and high- T disordered phases [39–41]. In Sec. IV, we provide a detailed quantitative analysis of the variation in conformational entropy (S_{conf}) associated with the OD phase transition in NPG. In this section, we concentrate on the molecular conformational differences between the ordered and disordered phases.

An NPG molecule can undergo conformational changes through internal rotations around its C—C, C—O, and O—H bond axes. To identify and quantify the population of molecules in the most predominant conformations, we define two dihedral angles, α and β , which are determined by the intersection of two flat surfaces. The first dihedral angle, α , is defined by two planes: one containing the oxygen atom of a hydroxyl group (O1), the carbon atom bonded to O1 (C1), and the carbon atom bonded to C1 (C2); and another containing the C1 and C2 atoms, along with the carbon atom bonded to the oxygen atom of the second hydroxyl group (C3) [Fig. 5(a)]. Similarly, the second dihedral angle, β , is defined by the plane containing the C1, C2, and C3 atoms, and the plane containing the C2 and C3 atoms along with the oxygen atom of the second hydroxyl group [i.e., the one closer to C3; see Fig. 5(a)].

A histogram of the two dihedral angles, α and β , provides a detailed characterization of molecular conformations in NPG, akin to the Ramachandran plots used in biochemistry for proteins [60]. We have generated conformational maps for both the low- T ordered [Fig. 5(b)] and high- T disordered [Fig. 5(c)] phases. In the ordered phase, two high-probability regions are evident, which could initially be interpreted as distinct molecular conformations. However, symmetry considerations reveal that these regions represent the same molecular conformation [Fig. 5(b)], differing only by a rotational transformation.

In the high- T disordered phase, the number of high-probability regions increases substantially, with eight distinct spots observed, indicating a broader variety of molecular conformations. Nonetheless, symmetry arguments again reduce the number of unique conformations,

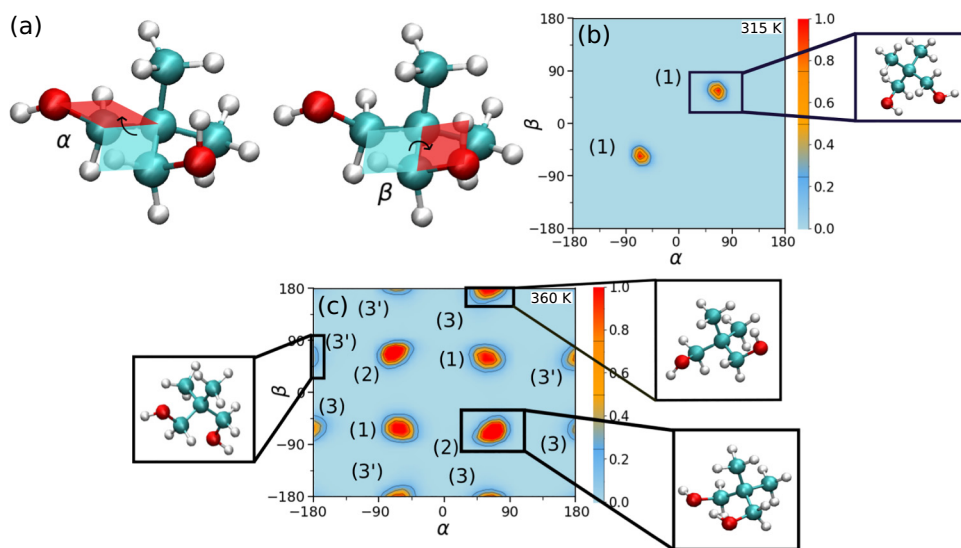


FIG. 5. The molecular conformational degrees of freedom in the ordered and disordered phases of NPG. (a) A representation of the two dihedral angles describing different NPG molecular conformations. (b), (c) Average dihedral angle histograms obtained from NPT -MD simulations for (b) the low- T (315 K) ordered and (c) high- T (360 K) disordered phases of NPG at zero pressure. The numbers on the figure indicate which high-probability spots describe equivalent or different molecular conformations.

as some spots correspond to equivalent configurations differentiated only by rotation. In particular, the eight high-probability regions reduce to four distinct molecular conformations in the orientationally disordered phase [labels 1, 2, 3, and 3' in Figs. 5(b), 5(c)].

It is worth noting that transitional paths connecting different conformations are absent for the high- T disordered phase [Fig. 5(c)], in contrast to the orientational diagrams presented in Figs. 4(c) and 4(e). This discrepancy arises because molecular conformational changes occur very rapidly, within a timescale shorter than 0.5 ps (i.e., the time interval used in this study for configuration sampling) and consequently are not captured.

E. Estimation of barocaloric effects in NPG

Using the computational approach detailed in Sec. II and the data presented in Figs. 3–5, we can estimate the total entropy of NPG as a function of temperature and pressure, $S(P, T)$, and particularly across its OD phase transition (without the need to explicitly calculate heat capacities [7,35]). Similar to quasidirect calorimetry experiments [8, 13,19,22], the barocaloric (BC) isothermal entropy change, ΔS_{BC} , and adiabatic temperature change, ΔT_{BC} , can be directly inferred from these entropy curves [7,35]. Specifically, ΔS_{BC} is calculated as $S(P, T) - S(0, T)$, while ΔT_{BC} is given by $T_0(P, S) - T(0, S)$, where T_0 satisfies the condition $S(P, T_0) = S(0, T)$. It is important to note that

hysteresis effects—often a significant limitation for practical applications [5,22]—are not considered in this study, as all the NPT -MD simulations have been conducted under thermodynamic equilibrium conditions.

In Fig. 6(a), we present the $S(P, T)$ curves calculated for NPG as a function of pressure and temperature. The computed BC isothermal entropy changes [Fig. 6(b)] accurately capture the expected increase in ΔS_{BC} under increasingly larger pressure shifts. Notably, the quantitative agreement between our calculated ΔS_{BC} values and the experimental data [19] is excellent within the numerical uncertainties [Fig. 6(c)]. For instance, for a pressure shift of 0.2 GPa, the calculated isothermal entropy change is $463 \text{ J K}^{-1} \text{ kg}^{-1}$, which aligns perfectly with the colossal experimental value of $450 \pm 25 \text{ J K}^{-1} \text{ kg}^{-1}$. This remarkable agreement extends across the entire range of investigated pressures. For example, at a pressure shift of 0.5 GPa, both the calculated and experimental ΔS_{BC} values converge at approximately $525 \text{ J K}^{-1} \text{ kg}^{-1}$ [Fig. 6(c)].

In Fig. 6(d), we illustrate the adiabatic temperature changes estimated for NPG, obtained directly from the $S(P, T)$ curves shown in Fig. 6(a). Consistent with the ΔS_{BC} results, our NPT -MD simulations and thermodynamic data analysis accurately reproduce the increasing trend of ΔT_{BC} under increasingly larger pressure shifts. For instance, the maximum ΔT_{BC} evaluated for a pressure shift of 0.1 GPa is 10 K, while for 0.5 GPa the maximum value reaches approximately 35 K [Fig. 6(d)].

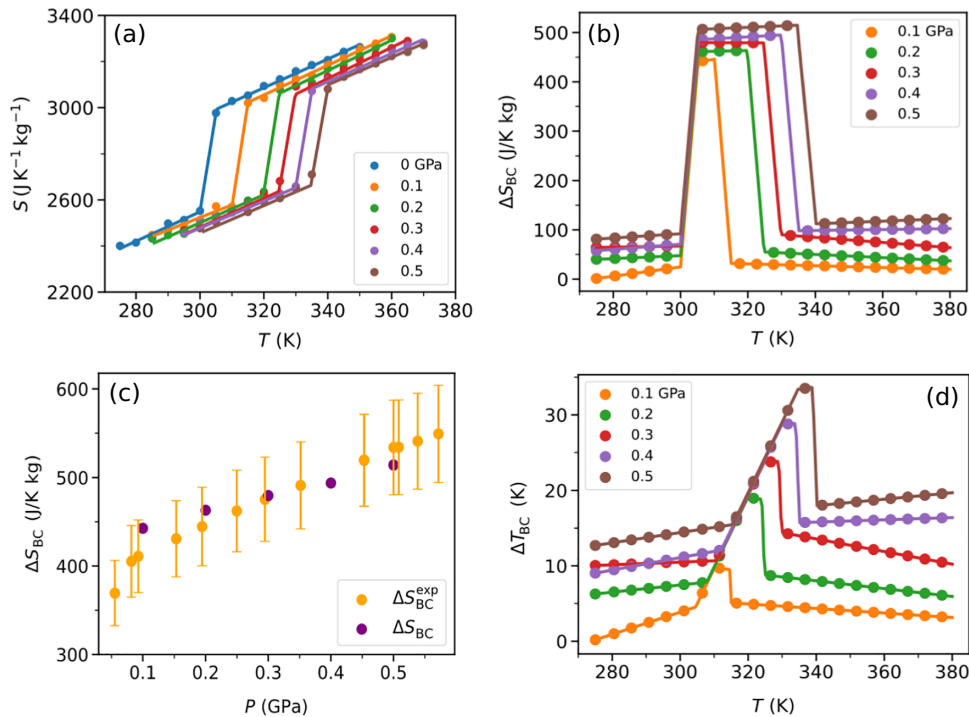


FIG. 6. The estimated BC performance of NPG. (a) Entropy curves expressed as a function of temperature at different fixed pressures. (b) Estimated BC isothermal entropy changes in NPG. (c) A comparison between the experimental and theoretical BC isothermal entropy changes. (d) The estimated BC adiabatic temperature changes in NPG. The solid lines are guides for the eye.

These estimations align closely with the corresponding experimental values of 11 K and 40 K [19], respectively.

IV. DISCUSSION

In the previous section, we have shown that the computational approach introduced in Sec. II, combined with the results of our comprehensive *NPT*-MD simulations, provides a quantitatively precise description of the OD phase transformation in NPG, whether driven by pressure or temperature, along with its distinctive BC performance as compared to experiments. To the best of our knowledge, this marks the first instance in which a classical simulation study based on a force field has achieved such a high degree of accuracy and quantification. This unique capability allows us to evaluate and compare the individual contributions to the phase-transition entropy change (ΔS_t) and BC isothermal entropy change (ΔS_{BC}) in NPG, as we proceed to do next.

In Figs. 7(a)–7(c), we illustrate the partial contributions to the total entropy—vibrational (S_{vib}), orientational (S_{ori}), and conformational (S_{conf})—for some selected pressure and temperature points. Together, these three contributions combine to produce the $S(P, T)$ curves shown in Fig. 6(a). In all cases, a significant increase in entropy is observed at the transition temperature corresponding to each pressure,

$T_t(P)$. The vibrational entropy, S_{vib} , increases monotonically with temperature and exhibits large values even far from the phase-transition region. In contrast, the two angular entropies, S_{ori} and S_{conf} , remain mostly negligible at temperatures below $T_t(P)$ and increase abruptly at the phase transition. Notably, the largest phase-transition entropy change originates from S_{ori} , which alone is already colossal (i.e., $\Delta S_t^{\text{ori}} \geq 100 \text{ J K}^{-1} \text{ kg}^{-1}$). However, the combined contributions of ΔS_t^{vib} and ΔS_t^{conf} are comparable in magnitude to ΔS_t^{ori} , thus emphasizing their importance in the total entropy change.

For a pressure shift of 0.2 GPa, the isothermal entropy change attributable solely to molecular reorientations, $\Delta S_{BC}^{\text{ori}}$, is approximately $240 \text{ J K}^{-1} \text{ kg}^{-1}$ [Fig. 7(b)]. Similarly, the isothermal entropy change arising from molecular conformational changes, $\Delta S_{BC}^{\text{conf}}$, is $110 \text{ J K}^{-1} \text{ kg}^{-1}$ [Fig. 7(c)]. Finally, the vibrational contribution to the total isothermal entropy change is $\Delta S_{BC}^{\text{vib}} = 100 \text{ J K}^{-1} \text{ kg}^{-1}$ [Fig. 7(a)]. Consequently, in relative terms, molecular reorientations account for approximately 53% of the BC response of NPG, while molecular conformations and vibrational contributions represent 25% and 22%, respectively. Analogous quantitative results are obtained for other pressure shifts [i.e., 0.4 GPa in Figs. 7(a)–7(c)].

In Fig. 7(d), we depict the relative contributions of the different entropy components to ΔS_t as a function of

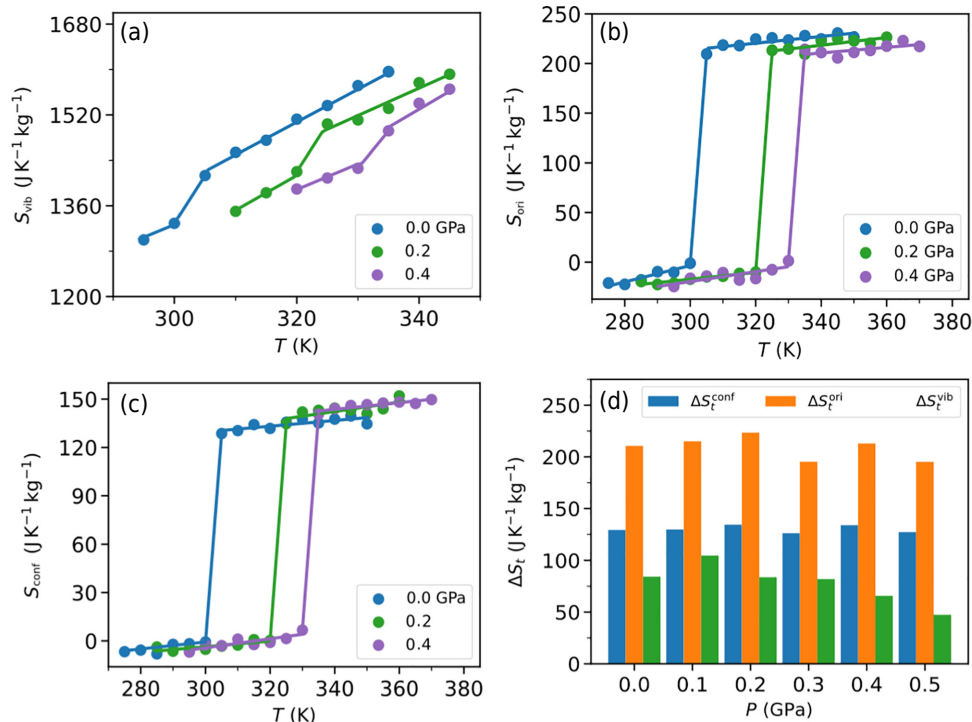


FIG. 7. (a)–(c) The vibrational, orientational, and conformational contributions to the entropy and transition entropy change in NPG: the (a) vibrational (vertical lines mark the phase-transition temperature corresponding to each pressure), (b) orientational, and (c) conformational entropies expressed as a function of temperature and pressure. (d) The contributions to the transition entropy change, expressed as a function of pressure. The solid lines are guides for the eye.

TABLE I. The phase-transition entropy change and partial contributions. Experimental (ΔS_t^{exp}) and theoretical (ΔS_{t_1} , ΔS_{t_2} and ΔS_t) values are shown for comparison. ΔS_{t_1} has been calculated using the Clausius-Clapeyron method and ΔS_{t_2} via the Gibbs free-energy equality [Sec. III A and Eq. (15)]. ΔS_t has been obtained as the sum of vibrational (ΔS_t^{vib}), orientational (ΔS_t^{ori}), and conformational (ΔS_t^{conf}) contributions [Eq. (3)]. The numerical uncertainties are indicated within parentheses.

P (GPa)	ΔS_t^{exp} (J K ⁻¹ kg ⁻¹)	ΔS_{t_1} (J K ⁻¹ kg ⁻¹)	ΔS_{t_2} (J K ⁻¹ kg ⁻¹)	ΔS_t (J K ⁻¹ kg ⁻¹)	ΔS_t^{vib} (J K ⁻¹ kg ⁻¹)	ΔS_t^{ori} (J K ⁻¹ kg ⁻¹)	ΔS_t^{conf} (J K ⁻¹ kg ⁻¹)
0.0	383 (40)	600 (240)	402 (15)	424 (25)	84 (10)	211 (20)	129 (20)
0.1	389 (40)	668 (320)	425 (15)	450 (25)	105 (10)	215 (20)	130 (20)
0.2	383 (40)	756 (430)	407 (15)	443 (25)	84 (10)	224 (20)	135 (20)
0.3	365 (40)	821 (560)	391 (15)	403 (25)	82 (10)	195 (20)	126 (20)
0.4	343 (40)	809 (660)	376 (15)	413 (25)	66 (10)	213 (20)	134 (20)
0.5	321 (40)	671 (650)	346 (15)	369 (25)	47 (10)	195 (20)	127 (20)

compression. At zero pressure, the dominant contributor is ΔS_t^{ori} , accounting for approximately 50% of the total entropy change. Notably, the ΔS_t^{conf} contribution, often overlooked in previous studies analyzing phase-transition entropy changes in plastic crystals [29–32], constitutes a significant 30%. The vibrational degrees of freedom, ΔS_t^{vib} , contribute the remaining 20%. At the highest investigated pressure, 0.5 GPa, the relative contributions remain consistent, with ΔS_t^{ori} amounting to 53%, ΔS_t^{conf} increasing slightly to 34%, and ΔS_t^{vib} decreasing to 13%. The values of these partial ΔS_t contributions are consistent with those reported above for ΔS_{BC} .

Table I lists the phase-transition entropy change values shown in Fig. 7(d), along with their numerical uncertainties. Notably, the ΔS_t values obtained by summing the partial vibrational, orientational, and conformational contributions are in excellent agreement with both the experimental measurements and the values computed directly from the *NPT*-MD simulations via the Gibbs-free-energy equality [i.e., ΔS_{t_2} , Sec. III A and Fig. 2(d)]. This consistency across independent computational and experimental approaches provides strong evidence that our entropy-decomposition framework is both physically meaningful and correctly implemented. Indeed, any significant discrepancies between ΔS_t and ΔS_{t_2} would cast serious doubt on the validity of our method; the absence of such discrepancies reinforces its reliability and robustness.

It is noteworthy that a previous study has provided a tentative estimation of the vibrational and angular (i.e., orientational and conformational together) contributions to ΔS_t for NPG, based on straightforward thermodynamic and molecular symmetry arguments [19]. Using the experimental values for the OD phase-transition volume change, the isobaric thermal expansion coefficient, and the isothermal compressibility averaged over the ordered and disordered phases, the authors have estimated $\Delta S_t^{\text{vib}} \approx 60 \text{ J K}^{-1} \text{ kg}^{-1}$ at zero pressure. This value is approximately 25% smaller than the vibrational contribution reported in this work [i.e., $80 \text{ J K}^{-1} \text{ kg}^{-1}$; see Fig. 7(d)]. Similarly, by considering up to 60 distinct and equally probable

configurations per NPG molecule in the disordered phase (i.e., 10 molecular orientations \times 6 possible conformations) and one in the ordered phase, they have estimated $\Delta S_t^{\text{ori+conf}} = M^{-1} R \ln(60) \approx 330 \text{ J K}^{-1} \text{ kg}^{-1}$, where $M = 104.15 \text{ g mol}^{-1}$ and R is the universal gas constant. This value aligns closely with our numerical result of $320 \text{ J K}^{-1} \text{ kg}^{-1}$ [Fig. 7(d)].

One of the approximations adopted throughout this work is that the molecular orientational and conformational degrees of freedom in NPG are effectively decoupled (Sec. II A). This assumption is supported by previous studies on similar molecular systems, which have shown that higher-order mixed contributions to the angular entropy are typically small [46,47]. Additionally, this approximation enhances computational efficiency. To quantitatively assess the magnitude of the orientation-conformation entropy cross term, we have followed the methodology described in Refs. [46,47,54,55] and applied it to the atomistic trajectories obtained at a temperature just above T_t and under zero-pressure conditions. Our analysis has revealed that this mixed contribution accounts for only 0.6% of the total angular entropy. Thus, its neglect in the present study is fully justified.

In Fig. 8, we present the time evolution of the two dihedral angles, α and β , which describe the molecular conformation, and the three Euler angles, θ , ϕ , and ψ , which define the molecular orientation, at a temperature just above T_t and under zero-pressure conditions. As shown in the figure, the conformational angles exhibit significantly lower frequencies of change compared to the orientational angles. Over a relatively long simulation interval of 0.5 ns, the dihedral angles undergo only one or two transitions, whereas the Euler angles display much more frequent variations. Moreover, direct inspection of Fig. 8 reveals a qualitative difference in the nature of these angular dynamics: conformational changes occur sporadically and are relatively abrupt, while molecular orientations evolve more continuously, characterized by smooth angular diffusion interspersed with discrete jumps. These pronounced differences in temporal behavior strongly suggest

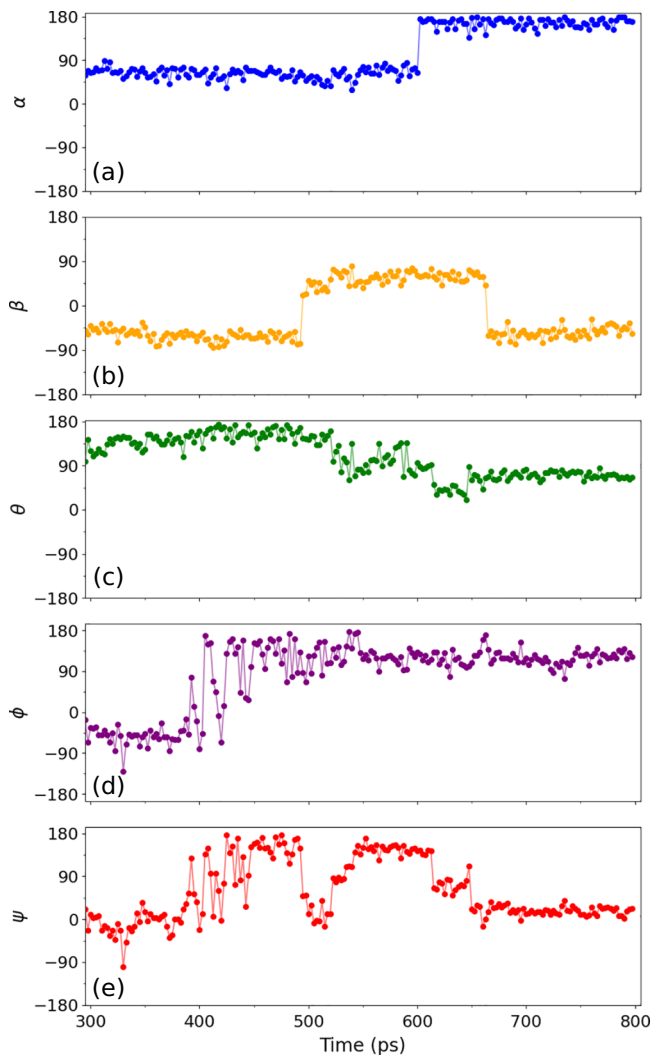


FIG. 8. The time evolution of the conformational and orientational degrees of freedom of NPG molecules: (a),(b) the conformational angles; (c)–(e) the orientational angles. The results have been obtained from an *NPT*-MD simulation performed at zero-pressure conditions and $T = 305$ K.

the absence of significant dynamical coupling between the conformational and orientational degrees of freedom in NPG molecules. This observation is consistent with the numerically negligible magnitude of the computed orientation-conformation entropy cross term.

The primary conclusion of this classical simulation study, based on the results presented in Fig. 7, is that across the OD phase transition in NPG, the combined entropy change from lattice vibrations and molecular conformations is comparable in magnitude to that resulting from molecular reorientations. Notably, within the former contributions, molecular conformations exhibit the largest entropy change. These findings, obtained from the archetypal plastic crystal NPG, are likely to be broadly applicable to other similar compounds.

Importantly, while hydrogen bonding—which directly affects molecular rotational dynamics in plastic crystals [33]—has traditionally been central to explaining the microscopic origins of the colossal BC effects observed in NPG and similar materials [29,30], the findings of this study suggest an expanded perspective. Our atomistic simulations demonstrate that molecular structural and lattice vibrational contributions together play an equally significant role. These factors should therefore be integrated into the rational engineering of plastic materials for solid-state cooling. Furthermore, incorporating molecular conformational and vibrational degrees of freedom into phenomenological free-energy models [31,32] also appears to be essential for achieving reliable descriptions of BC performance in plastic crystals.

V. CONCLUSIONS

In this study, we elucidate the molecular mechanisms underpinning the colossal barocaloric effects observed in the plastic crystal neopentyl glycol using molecular dynamics simulations and advanced entropy-evaluation methods. Our results reveal that the entropy changes associated with molecular reorientations, lattice vibrations, and conformational degrees of freedom are all significant and collectively contribute to the barocaloric performance of NPG. Notably, we establish that the joint contributions from lattice vibrations and molecular conformations are comparable to those from molecular reorientations, challenging the conventional view that rotational dynamics alone dominate such effects.

Furthermore, our simulation results demonstrate excellent agreement with experimental data, both in terms of phase-transition entropy changes and barocaloric performance metrics, validating the accuracy of our computational approach. These findings emphasize the need to incorporate vibrational and conformational contributions into the rational design and modeling of advanced barocaloric materials. By broadening the understanding of entropy mechanisms in plastic crystals, this work provides valuable insights for developing next-generation solid-state cooling technologies with improved efficiency and functionality.

VI. METHODS

A. Molecular dynamics simulations

We have used the GROMACS simulation code [61] to perform systematic classical MD simulations in the *NPT* ensemble for bulk NPG using a CHARMM-type force field [42–44] (see the Supplemental Material [45]). The average temperature and pressure values have been set using Nosé-Hoover thermostats and barostats with a mean fluctuation of 5 K and 0.01 GPa, respectively. The simulation box contained a total of 4104 atoms (equivalent to 216 NPG

molecules) and periodic boundary conditions have been applied along the three Cartesian directions. The long-range electrostatic interactions have been calculated by using a particle-particle particle-mesh solver to compute Ewald sums up to an accuracy of 10^{-4} kcal mol $^{-1}$ Å $^{-1}$ in the atomic forces. The cutoff distance for evaluation of the potential energy was 12 Å.

To determine the phase-transition temperature of NPG under broad pressure conditions, we have conducted comprehensive *NPT*-MD simulations in the temperature range $200 \leq T \leq 400$ K, taken at intervals of 5 K. In our *NPT*-MD simulations, the temperature and pressure have been steadily increased up to targeted values over 1 ns. Subsequently, the system has been equilibrated at the selected conditions for 1 ns. The production runs have then lasted for about 500 ps using a time step of 2 fs, from which the velocities of the atoms and other key quantities (e.g., the potential energy and volume of the system) have been extracted. From the production *NPT*-MD runs, a total of 1000 equispaced configurations have been retrieved to obtain uncorrelated structural data and generate accurate angular probability densities and histograms.

B. Molecular angular and entropy analysis

The NPG angular degrees of freedom have been retrieved from the atomic configurations generated during the *NPT*-MD simulations with the help of the in-house developed, freely available and open-source software ANGULA [62]. ANGULA is designed to automatically and unsupervisedly determine the angles defining the orientational structure of molecular disordered crystals from data files containing their atomic positions. Among its many capabilities, ANGULA can generate angular probability density maps and directional radial distribution functions directly from sequences of molecular configurations. In this study, the angular molecular entropy terms S_{ori} and S_{conf} have been directly computed from the outputs of our *NPT*-MD simulations using ANGULA [62].

ACKNOWLEDGMENTS

We acknowledge financial support from the Spanish Ministry of Science and Innovation through Grant No. MCIN/AEI/10.13039/501100011033, from the European Union European Regional Development Fund (ERDF) under Project No. PID2023-146623NB-I00, and through the “María de Maeztu” Program for Units of Excellence (CEX2023-001300-M), as well as from the Generalitat de Catalunya (Grant No. 2021SGR-00343). C.C. also acknowledges financial support from MCIN/AEI/10.13039/501100011033 under the “Ramón y Cajal” fellowship RYC2018-024947-I and Grant No. TED2021-130265B-C22. J.-L.I.T. is grateful to the ICREA

Academia program. We also thankfully acknowledge technical support and computational resources at MareNostrum5 provided by the Barcelona Supercomputing Center (Grants No. FI-2023-1-0002, No. FI-2023-2-0004, No. FI-2023-3-0004, No. FI-2024-1-0005, and No. FI-2024-2-0003).

DATA AVAILABILITY

The data that support the findings of this paper are not publicly available because they contain commercially sensitive information. The data are available from the authors upon reasonable request.

-
- [1] Ll. Mañosa, A. Planes, and M. Acet, Advanced materials for solid-state refrigeration, *J. Mater. Chem. A* **1**, 4925 (2013).
 - [2] Ll. Mañosa, D. González-Alonso, A. Planes, E. Bonnot, M. Barrio, J.-Ll. Tamarit, S. Aksoy, and M. Acet, Giant solid-state barocaloric effect in the Ni-Mn-In magnetic shape-memory alloy, *Nat. Mater.* **9**, 478 (2010).
 - [3] Ll. Mañosa and A. Planes, Materials with giant mechanocaloric effects: Cooling by strength, *Adv. Mater.* **29**, 1603607 (2017).
 - [4] C. Cazorla, Novel mechanocaloric materials for solid-state cooling applications, *Appl. Phys. Rev.* **6**, 041316 (2019).
 - [5] P. Lloveras and J.-Ll. Tamarit, Advances and obstacles in pressure-driven solid-state cooling: A review of barocaloric materials, *MRS Energy Sustain.* **8**, 3 (2021).
 - [6] H. Hou, S. Qian, and I. Takeuchi, Materials, physics and systems for multicaloric cooling, *Nat. Rev. Mater.* **7**, 633 (2022).
 - [7] R. Rurali, C. Escorihuela-Sayalero, J.-Ll. Tamarit, J. Íñiguez-González, and C. Cazorla, Giant photocaloric effects across a vast temperature range in ferroelectric perovskites, *Phys. Rev. Lett.* **133**, 116401 (2024).
 - [8] A. Aznar, P. Lloveras, M. Romanini, M. Barrio, J.-Ll. Tamarit, C. Cazorla, D. Errandonea, N. D. Mathur, A. Planes, X. Moya, and Ll. Mañosa, Giant barocaloric effects over a wide temperature range in superionic conductor AgI, *Nat. Commun.* **8**, 1851 (2017).
 - [9] C. Cazorla and D. Errandonea, Giant mechanocaloric effects in fluorite-structured superionic materials, *Nano Lett.* **16**, 3124 (2016).
 - [10] A. K. Sagotra, D. Errandonea, and C. Cazorla, Mechanocaloric effects in superionic thin films from atomistic simulations, *Nat. Commun.* **8**, 963 (2017).
 - [11] A. K. Sagotra, D. Chu, and C. Cazorla, Room-temperature mechanocaloric effects in lithium-based superionic materials, *Nat. Commun.* **9**, 3337 (2018).
 - [12] Ll. Mañosa and A. Planes, Solid-state cooling by stress: A perspective, *Appl. Phys. Lett.* **116**, 050501 (2020).
 - [13] P. Lloveras, *Barocaloric Effects in the Solid State: Materials and Methods* (IOP Publishing, 2023).
 - [14] S. L. Piper, L. Melag, M. Kar, A. Sourjah, X. Xiao, E. F. May, K.-F. Aguey-Zinsou, D. R. Macfarlane, and J.

- M. Pringle, Organic ionic plastic crystals having colossal barocaloric effects for sustainable refrigeration, *Science* **387**, 56 (2025).
- [15] F. Li, C. Niu, X. Xu, M. Li, and H. Wang, The effect of defect and substitution on barocaloric performance of neopentylglycol plastic crystals, *Appl. Phys. Lett.* **121**, 223902 (2022).
- [16] K. Zhang, Z. Zhang, H. Pan, H. Wang, X. Zhao, J. Qi, Z. Zhang, R. Song, C. Yu, B. Huang *et al.*, Taming heat with tiny pressure, *The Innovation* **5**, 100577 (2024).
- [17] X. Xu, F. Li, C. Niu, M. Li, and H. Wang, Machine learning assisted investigation of the barocaloric performance in ammonium iodide, *Appl. Phys. Lett.* **122**, 043901 (2023).
- [18] Z. Zhang, X. Jiang, T. Hattori, X. Xu, M. Li, C. Yu, Z. Zhang, D. Yu, R. Mole, S.-i. Yano *et al.*, A colossal barocaloric effect induced by the creation of a high-pressure phase, *Mater. Horiz.* **10**, 977 (2023).
- [19] P. Lloveras, A. Aznar, M. Barrio, Ph. Negrier, C. Popescu, A. Planes, Ll. Mañosa, E. Stern-Taulats, A. Avramenko, N. D. Mathur *et al.*, Colossal barocaloric effects near room temperature in plastic crystals of neopentylglycol, *Nat. Commun.* **10**, 1803 (2019).
- [20] B. Li, Y. Kawakita, S. Ohira-Kawamura, T. Sugahara, H. Wang, J. Wang, Y. Chen, S. I. Kawaguchi, S. Kawaguchi, K. Ohara *et al.*, Colossal barocaloric effects in plastic crystals, *Nature* **567**, 506 (2019).
- [21] C. Cazorla, Refrigeration based on plastic crystals, *Nature* **567**, 470 (2019).
- [22] A. Aznar, P. Lloveras, M. Barrio, P. Negrier, A. Planes, Ll. Mañosa, N. D. Mathur, X. Moya, and J.-Ll. Tamarit, Reversible and irreversible colossal barocaloric effects in plastic crystals, *J. Mater. Chem. A* **8**, 639 (2020).
- [23] A. Aznar, P. Negrier, A. Planes, Ll. Mañosa, E. Stern-Taulats, X. Moya, M. Barrio, J.-Ll. Tamarit, and P. Lloveras, Reversible colossal barocaloric effects near room temperature in 1-X-adamantane (X=Cl, Br) plastic crystals, *Appl. Mater. Today* **23**, 101023 (2021).
- [24] A. Salvatori, P. Negrier, A. Aznar, M. Barrio, J.-Ll. Tamarit, and P. Lloveras, Colossal barocaloric effects in adamantane derivatives for thermal management, *APL Mater.* **10**, 111117 (2022).
- [25] K. Zhang, R. Song, J. Qi, Z. Zhang, Z. Zhang, C. Yu, K. Li, Z. Zhang, and B. Li, Colossal barocaloric effect in carboranes as a performance tradeoff, *Adv. Funct. Mater.* **32**, 2112622 (2022).
- [26] K. Sau, T. Ikeshoji, S. Takagi, S.-i. Orimo, D. Errandonea, D. Chu, and C. Cazorla, Colossal barocaloric effects in the complex hydride $\text{Li}_2\text{B}_{12}\text{H}_{12}$, *Sci. Rep.* **11**, 11915 (2021).
- [27] M. Zeng, C. Escorihuela-Sayalero, T. Ikeshoji, S. Takagi, S. Kim, S.-i. Orimo, M. Barrio, J.-Ll. Tamarit, P. Lloveras, C. Cazorla, and K. Sau, Colossal reversible barocaloric effects in a plastic crystal mediated by lattice vibrations and ion diffusion, *Adv. Sci.* **11**, 2306488 (2024).
- [28] L. Cirillo, A. Greco, and C. Masselli, Cooling through barocaloric effect: A review of the state of the art up to 2022, *Therm. Sci. Eng. Prog.* **33**, 101380 (2022).
- [29] F. B. Li, M. Li, C. Niu, and H. Wang, Atomic-scale insights into the colossal barocaloric effects of neopentyl glycol plastic crystals, *Appl. Phys. Lett.* **120**, 073902 (2022).
- [30] F. B. Li, M. Li, X. Xu, Z. C. Yang, H. Xu, C. K. Jia, K. Li, J. He, B. Li, and H. Wang, Understanding colossal barocaloric effects in plastic crystals, *Nat. Commun.* **11**, 4190 (2020).
- [31] N. de Oliveira, Barocaloric effect in neopentylglycol plastic crystal: A theoretical study, *Acta Mater.* **246**, 118657 (2023).
- [32] R. Marín-Delgado, X. Moya, and G. G. Guzmán-Verri, Landau theory of barocaloric plastic crystals, *J. Phys. Energy* **6**, 035003 (2024).
- [33] J.-Ll. Tamarit and M. A. Pérez-Jubindo, Dielectric studies on orientationally disordered phases of neopentylglycol and tris(hydroxymethyl aminomethane), *J. Phys.: Condens. Matter* **9**, 5469 (1997).
- [34] C. Escorihuela-Sayalero, A. Sanuy, L. C. Pardo, and C. Cazorla, Orientational disorder and molecular correlations in hybrid organic-inorganic perovskites: From fundamental insights to technological applications, *ACS Appl. Mater. Interfaces* **17**, 1428 (2025).
- [35] C. Escorihuela-Sayalero, L. C. Pardo, M. Romanini, N. Obrecht, S. Loehlé, P. Lloveras, J.-Ll. Tamarit, and C. Cazorla, Prediction and understanding of barocaloric effects in orientationally disordered materials from molecular dynamics simulations, *Npj Comput. Mater.* **10**, 13 (2024).
- [36] B. E. Meijer, R. J. C. Dixey, F. Demmel, R. Perry, H. C. Walker, and A. E. Phillips, Dynamics in the ordered and disordered phases of barocaloric adamantane, *Phys. Chem. Chem. Phys.* **25**, 9282 (2023).
- [37] S. Yuan, B. E. Meijer, G. Cai, R. J. C. Dixey, F. Demmel, M. T. Dove, J. Liu, H. Y. Playford, H. C. Walker, and A. E. Phillips, Origin of the large entropy change in the molecular caloric and ferroelectric ammonium sulfate, *Adv. Funct. Mater.* **32**, 2207717 (2022).
- [38] A. E. Phillips and H. C. Walker, On (not) deriving the entropy of barocaloric phase transitions from crystallography and neutron spectroscopy, *J. Phys. Energy* **6**, 011001 (2024).
- [39] J. Seo, R. D. McGillicuddy, A. H. Slavney, S. Zhang, R. Ukani, A. A. Yakovenko, S.-L. Zheng, and J. A. Mason, Colossal barocaloric effects with ultralow hysteresis in two-dimensional metal-halide perovskites, *Nat. Commun.* **13**, 2536 (2022).
- [40] J. Li, M. Barrio, D. J. Dunstan, R. Dixey, X. Lou, J.-Ll. Tamarit, A. E. Phillips, and P. Lloveras, Colossal reversible barocaloric effects in layered hybrid perovskite $(\text{C}_{10}\text{H}_{21}\text{NH}_3)_2\text{MnCl}_4$ under low pressure near room temperature, *Adv. Funct. Mater.* **31**, 2105154 (2021).
- [41] J. Seo, R. Ukani, J. Zheng, J. D. Braun, S. Wang, F. E. Chen, C. Thai, and R. D. McGillicuddy *et al.*, Barocaloric effects in dialkylammonium halide salts, *J. Am. Chem. Soc.* **146**, 2736 (2024).
- [42] B. R. Brooks, C. L. Brooks III, A. D. Mackerell, L. Nilsson, R. J. Petrella, B. Roux, Y. Won, G. Archontis, C. Bartels, and S. Boresch *et al.*, CHARMM: The biomolecular simulation program, *J. Comp. Chem.* **30**, 1545 (2009).
- [43] V. Zoete, M. A. Cuendet, A. Grosdidier, and O. Michielin, SwissParam: A fast force field generation tool for small organic molecules, *J. Comput. Chem.* **32**, 2359 (2011).
- [44] M. Bugnon, M. Goullieux, U. F. Röhrig, M. A. S. Perez, A. Daina, O. Michielin, and V. Zoete, SwissParam 2023: A modern web-based tool for efficient small molecule parametrization, *J. Chem. Inf. Model.* **63**, 6469 (2023).

- [45] See the Supplemental Material at <http://link.aps.org/supplemental/10.1103/bknr-9rnn> for a detailed description of the CHARMM-type force field used to perform systematic NPT-MD simulations of bulk NPG.
- [46] A. Henao, S. Busch, E. Guàrdia, J.-Ll. Tamarit, and L. C. Pardo, The structure of liquid water beyond the first hydration shell, *Phys. Chem. Chem. Phys.* **18**, 19420 (2016).
- [47] L. C. Pardo, A. Henao, and A. Vispa, Characterizing ordering in liquids: An information theoretic approach, *J. Non-Cryst. Solids* **407**, 220 (2015).
- [48] D. J. Huggins, Estimating translational and orientational entropies using the k -nearest neighbors algorithm, *J. Chem. Theory Comput.* **10**, 3617 (2014).
- [49] A. K. Sagotra, D. Chu, and C. Cazorla, Influence of lattice dynamics on lithium-ion conductivity: A first-principles study, *Phys. Rev. Mater.* **3**, 035405 (2019).
- [50] C. López, A. Emperador, E. Saucedo, R. Rurali, and C. Cazorla, Universal ion-transport descriptors and classes of inorganic solid-state electrolytes, *Mater. Horiz.* **10**, 1757 (2023).
- [51] C. Cazorla and J. Boronat, Simulation and understanding of atomic and molecular quantum crystals, *Rev. Mod. Phys.* **89**, 035003 (2017).
- [52] T. M. Cover and J. A. Thomas, *Elements of Information Theory*, (Wiley Series in Telecommunications and Signal Processing) (Wiley-Interscience, Hoboken, New Jersey, 2006).
- [53] R. Pathria, *Statistical Mechanics*, Elsevier Science and Technology Books (Boston, 1972).
- [54] T. Lazaridis and M. Karplus, Orientational correlations and entropy in liquid water, *J. Chem. Phys.* **105**, 4294 (1996).
- [55] H. Matsuda, Physical nature of higher-order mutual information: Intrinsic correlations and frustration, *Phys. Rev. E* **62**, 3096 (2000).
- [56] R. Zanetti, The unit cell and space group of 2,2 dimethyl-1,3 propanediol, *Act. Cryst.* **14**, 203 (1961).
- [57] J. P. Heremans, V. Jovovic, E. S. Toberer, A. Saramat, K. Kurosaki, A. Charoenphakdee, S. Yamanaka, and G. J. Snyder, Enhancement of thermoelectric efficiency in PbTe by distortion of the electronic density of states, *Science* **321**, 554 (2008).
- [58] H. R. Clyde and M. L. Klein, Anharmonic effects and the lattice dynamics of insulators, *CRC Crit. Rev. Solid State Mater.* **2**, 181 (1971).
- [59] B. Granzow, P. Klaeboe, and V. Sablinskas, Molecular spectroscopic studies and *ab initio* calculations of four alcohols derived from 2,2-dimethylpropane, *J. Mol. Struct.* **349**, 153 (1995).
- [60] G. N. Ramachandran, C. Ramakrishnan, and V. Sasisekharan, Stereochemistry of polypeptide chain configurations, *J. Mol. Biol.* **7**, 95 (1963).
- [61] M. J. Abraham, T. Murtola, R. Schulz, S. Páll, J. C. Smith, B. Hess, and E. Lindahl, GROMACS: High performance molecular simulations through multi-level parallelism from laptops to supercomputers, *SoftwareX* **1**, 19 (2015).
- [62] <https://gcm.upc.edu/en/members/luis-carlos/angula/> ANGULA.